J. Fluid Mech. (2007), *vol.* 580, *pp.* 123–143.
doi:10.1017/S0022112007005289 Printed in the United Kingdom

Experimental and numerical studies of magnetoconvection in a rapidly rotating spherical shell

N. GILLET†, D. BRITO, D. JAULT AND H.-C. NATAF

Laboratoire de Géophysique Interne et Tectonophysique, CNRS, Observatoire de Grenoble, Université Joseph–Fourier, Maison des Géosciences, BP 53, 38041 Grenoble Cedex 09, France

(Received 3 July 2006 and in revised form 28 November 2006)

Thermal magnetoconvection in a rapidly rotating spherical shell is investigated numerically and experimentally in electrically conductive liquid gallium (Prandtl number $P = 0.025$), at Rayleigh numbers R up to around 6 times critical and at Ekman numbers $E \sim 10^{-6}$. This work follows up the non-magnetic study of convection presented in a companion paper (Gillet *et al.* 2007). We study here the addition of a z-invariant toroidal magnetic field to the fluid flow. The experimental measurements of fluid velocities by ultrasonic Doppler velocimetry, together with the quasi-geostrophic numerical simulations incorporating a three-dimensional modelling of the magnetic induction processes, demonstrate a stabilizing effect of the magnetic field in the weak-field case, characterized by an Elsasser number $\Lambda < (E/P)^{1/3}$. We find that this is explained by the changes of the critical parameters at the onset of convection as Λ increases. As in the non-magnetic study, strong zonal jets of characteristic length scales ℓ_β (Rhines length scale) dominates the fluid dynamics. A new characteristic of the magnetoconvective flow is the elongation of the convective cells in the direction of the imposed magnetic field, introducing a new length scale ℓ_ϕ. Combining experimental and numerical results, we derive a scaling law $\overline{U} \sim (\widetilde{U}_s \widetilde{U}_\phi)^{2/3} \sim \widetilde{U}_s{}^{4/3} (\ell_\phi/\ell_\beta)^{2/3}$ where $\overline{U}$ is the axisymmetric motion amplitude, $\widetilde{U}_s$ and $\widetilde{U}_\phi$ are the non-axisymmetric radial and azimuthal motion amplitudes, respectively.

1. Introduction

We present in Gillet *et al.* (2007) (hereafter referred as Part 1) a study of rapidly rotating nonlinear convection in a spherical shell, for both large and small Prandtl numbers $P = \nu/\kappa$ (ν and κ are the kinematic viscosity and the thermal diffusivity, respectively). Rapid rotation implies that at first order motions are invariant along the rotation axis $\hat{\boldsymbol{z}}$. We couple a centrifugal gravity experiment with a quasi-geostrophic numerical model including a varying Coriolis parameter, β, that describes the motions in the equatorial plane perpendicular to $\hat{\boldsymbol{z}}$. $\beta(s) = 2\eta/EH$ in its dimensionless form is equivalent to the latitudinal variation of the Coriolis parameter that enters the β-plane equations in shallow layer systems, with η the slope of the container boundary, H the half-height of the fluid column and $E = \nu/\Omega d^2$ the Ekman number (Ω is the rotation rate and d is the gap between the outer and inner boundaries). For $P \ll 1$ most of the kinetic energy is stored in large-scale retrograde zonal flows. Their amplitude $\overline{U}$

† Present address: The Department of Earth Sciences, University of Leeds, LS2 9JT Leeds, UK.

Definition [Units]	Symbol	Gallium	Earth's core
Density [$\mathrm{kg\,m^{-3}}$]	ρ	6.1×10^{3}	$\sim10^{4}$
Kinematic viscosity [$\mathrm{m^2\,s^{-1}}$]	ν	$2.9-3.2\times10^{-7}$	$\sim10^{-6}$
Thermal expansion coefficient [$\mathrm{K^{-1}}$]	α	1.3×10^{-4}	$\sim10^{-5}$
Thermal diffusivity [$\mathrm{m^2\,s^{-1}}$]	κ	1.3×10^{-5}	$\sim10^{-5}$
Magnetic diffusivity [$\mathrm{m^2\,s^{-1}}$]	λ	0.21	~1

TABLE 1. Physical properties of liquid gallium (Brito 1998) and their estimation for the Earth's core (Wijs *et al.* 1998; Secco & Schloessin 1989).

is much more intense than the amplitude of the non-axisymmetric radial motions $\widetilde{U}_s$ (definitions of the velocity norms are given in § 4). Assuming a Rhines length scale

$$\ell_\beta \sim \sqrt{\overline{U}/\beta(s)} \tag{1.1}$$

for the width of the zonal jets (equation (4.3), Part 1), we have proposed the scaling law

$$\overline{U} \sim \widetilde{U}_s{}^{4/3}, \tag{1.2}$$

independent of the rotation rate (equation (4.7), Part 1). The length scale ℓ_β emerges as a consequence of the reverse cascade of kinetic energy in β-plane turbulence (Rhines 1975).

In the present paper the impact of an imposed magnetic field on the fluid flow is investigated. We report an experimental study of nonlinear magnetoconvection in a rapidly rotating spherical shell filled with liquid gallium ($P=0.025$), the physical properties of which are summarized in table 1. The experimental study is backed by numerical simulations using the quasi-geostrophic assumption and a three-dimensional induction model. The apparatus described in Part 1 has been modified to impose a current-free azimuthal magnetic field. As in the non-magnetic study we use ultrasonic Doppler velocimetry to measure flow velocities in gallium. Ekman numbers E down to 10^{-6} and Rayleigh numbers $R=\gamma\alpha\Delta T d^4/\kappa\nu$ up to 6 times critical have been reached experimentally (α is the thermal expansion coefficient, γ is the centrifugal gravity gradient and ΔT is the temperature drop between the boundaries). We consider a parameter domain where

(i) the amplitude b of the magnetic field induced by the fluid motion is extremely small compared to the amplitude $\mathscr{B}$ of the imposed field, the magnetic Reynolds number $R_m=\mathscr{U}\ell/\lambda$ being extremely small compared to 1 ($\mathscr{U}$ and ℓ are typical amplitudes for the velocity field and the vortex length scales, respectively; λ is the magnetic diffusivity);

(ii) the Lorentz forces remain small in comparison with the Coriolis forces, as measured by the Elsasser number $\Lambda=\sigma\mathscr{B}^2/\rho\Omega$ (σ is the electrical conductivity of the moving fluid and ρ its density).

The marginal stability analysis of the rapidly rotating β-plane convection is characterized by a thermal Rossby wave (Busse 1970; Roberts 1968) whose critical values (Rayleigh number, wavenumber and pulsation) are governed by the modified Ekman number $E^*=(\nu+\kappa)/\Omega d^2$. In liquid metals where $P\ll1$ the thermal Ekman number $E_\kappa=E/P$ then becomes the control parameter. Soward (1979) and Fearn (1979*a*, *b*) presented marginal stability analyses of rotating magnetoconvection, describing how the thermal Rossby modes are modified as the Elsasser number

increases. They dissociate the modified Rossby modes for $\Lambda < E_\kappa^{1/3}$ from the magnetic or slow modes for $E_\kappa^{1/3} < \Lambda < O(1)$. These analyses have been confirmed and extended by the coupled analytical and numerical study of Jones, Mussa & Worland (2003).

Nonlinear magnetoconvection has also been explored in three-dimensional numerical studies, which often deal with relatively large Ekman and Prandtl numbers (e.g. Olson & Glatzmaier 1995, $E \geqslant 5 \times 10^{-5}$ and $P = 1$; Zhang 1999, $E \simeq 10^{-3}$) far from the range of parameters we aim to reach in this study. Cardin & Olson (1995) performed a parameter study using a quasi-geostrophic approximation approach, with varying $0.1 < \Lambda < 10$ and $E \geqslant 10^{-6}$ for $P = 7$, in the presence of an imposed magnetic field that is azimuthal and does not vary with the distance from the axis. Although fully three-dimensional nonlinear studies have required large E due to numerical limitations, it is of interest to compare numerical simulations to experiments in order to test the validity domain of numerical approaches. Comparison between simulations and experiments also provides a unique opportunity to evaluate the effect of very small magnetic Prandtl numbers $P_m = \nu/\lambda$ ($\simeq 10^{-6}$ for metallic fluids) in magnetohydrodynamic fluid flows, and possibly deduce a way to parameterize in numerical simulations the mechanisms associated with such a small number.

Few experimental studies of rotating magnetoconvection have been carried out, however. Following the early work by Chandrasekar (1954), who proposed a theoretical framework for the marginal instability problem, Nagakawa (1957, 1958) first studied the onset of convection in a plane layer of mercury in the presence of both rotation and a magnetic field. Aurnou & Olson (2001) reported heat-flux measurements in a similar experiment but with gallium. A limitation of plane layer convection is that it lacks an important physical ingredient of the planetary core dynamics: the presence of sloping boundaries. Only then are zonal motions set up and low-frequency Rossby waves can propagate. A few recent magnetoconvection experimental studies have included this feature: Jaletzky (1999) focused on the instability threshold in a rotating cylindrical annulus filled with a low-Prandtl-number liquid. Recently, Shew & Lathrop (2005) have used a larger (and more rapidly rotating) sphere filled with liquid sodium ($P \sim 0.01$) and investigated both convection and magnetoconvection in the nonlinear regime. Their data consist of measurements of the temperature perturbations and heat flux. They imposed a magnetic field aligned with the rotation axis $\hat{\boldsymbol{z}}$, with Λ up to $2 \times 10^{-4} \ll E_\kappa^{1/3}$. With increasing Elsasser numbers they mainly noticed a change in the heat transfer distribution – an increase in the equatorial region, together with a decrease at mid-latitude – which they analysed as the effect of the bi-dimensionalization of the flow along the imposed field lines.

Very little is known about the impact of the magnetic field on the quasi-geostrophic dynamics. In this respect, our work is part of an ongoing research program, that began with the experimental study of a single geostrophic vortex in gallium in a transverse magnetic field by Brito *et al.* (1995, 1996). They noticed both a decrease of the angular velocity and an increase of the vortex size as the Elsasser number increases towards unity. In the present study we consider the parameter regime where $\Lambda < E_\kappa^{1/3}$, the so-called weak-field case.

The organization of this paper is as follows. The experimental set-up is described in § 2.1. In § 2.2 we present a three-dimensional model of the experiment, and then in § 2.3 incorporate the Lorentz force into the quasi-geostrophic numerical model used in the non-magnetic case (Part 1). In § 3 we describe the effect of the magnetic field on the onset of convection. Then we compare in § 4 our magnetoconvection experiments to computations in the nonlinear regime. We describe how the presence of a toroidal

magnetic field modifies the scaling laws developed in Part 1. Finally our conclusions are presented in § 5. For convenience, both cylindrical polar $(\hat{\boldsymbol{s}}, \hat{\boldsymbol{\phi}}, \hat{\boldsymbol{z}})$ and spherical coordinates $(\hat{\boldsymbol{r}}, \hat{\boldsymbol{\theta}}, \hat{\boldsymbol{\phi}})$ are used throughout the description below.

2. The experimental and numerical models

2.1. *The experimental apparatus and measurement techniques*

The main characteristics of the experimental apparatus and measurement techniques used in this paper have already been presented in Part 1 (see also Aubert *et al.* 2001). We detail here how the experimental set-up has been adapted for magnetoconvection studies. In order to impose a magnetic field on the experiments, we have formed a solenoid from a copper wire that loops in and out of the inner cylinder and the outer sphere, as sketched in figure 1: the coils are distributed uniformly in longitude around the outer sphere. The solenoidal distribution of electrical currents imposes on the liquid gallium flow a z-invariant toroidal magnetic field, varying in intensity as $B(s) = (\mu_0 N I)/(2\pi s)$ for $s_i \leqslant s \leqslant r_o$, with μ_0 the permeability of free space, I the electrical intensity circulating in the copper wire (up to 14 A with a precision of 0.1 A) and $N = 444$ the number of loops. The intensity of the magnetic field can be increased up to 3×10^{-2} T near the inner cylinder. The boundaries of the fluid container are electrically insulating as there is a thin layer of cataphoresis (see Brito *et al.* 2001 and Aubert *et al.* 2001) between liquid gallium and the copper parts (outer sphere and central region of the inner cylinder).

In the only previously published experiment on nonlinear magnetoconvection incorporating a β-effect, Shew & Lathrop (2005) used a measurement technique based on the temperature perturbations in order to indirectly retrieve information on the velocity field. We use here ultrasonic Doppler velocimetry to directly measure velocities in gallium. An ultrasonic probe rotating with the sphere in the equatorial plane (see figures 1(a) and 2, Part 1) emits an intermittent 4 MHz signal and receives a signal that has been sent back by particles (gallium oxides). We assume that the velocity field is nearly z-invariant due to rapid rotation. We have access to two components of the velocity field from the ultrasonic measurements (see Part 1): the radial flow u_s, from which we build the r.m.s. velocity profile $\widetilde{U}_{\rm rad}(s) = (\langle [u_s - \langle u_s \rangle_\tau]^2 \rangle_\tau)^{1/2}$, and the mean azimuthal flow $\overline{u}_\phi$, from which we build the mean zonal velocity profile $\overline{U}_{\rm zon}(s) = \langle \overline{u}_\phi(s,t) \rangle_\tau$. We here denote by an overbar the average over ϕ, and by $\langle \ldots \rangle_\tau = (1/\tau) \int_\tau \ldots \mathrm{d}t$ the time average, where τ is typically a few hundred seconds. A more complete description of the data analysis is developed in Part 1 and Gillet (2004).

2.2. *Mathematical model of the experiments*

We model thermal magnetoconvection of a Boussinesq fluid between an outer sphere (spherical radius r_o) and a vertical inner cylinder (cylindrical radius s_i), in the presence of an imposed toroidal magnetic field $B(s)\hat{\boldsymbol{\phi}}$, the whole system rotating with a constant angular velocity $\Omega\,\hat{\boldsymbol{z}}$. In order to mimic the experiment, gravity is cylindrical and increases linearly in radius as γs where $\gamma = \Omega^2$. We use no-slip boundary conditions for the velocity field at the boundaries. The outer sphere is at constant temperature T_o. The inner cylinder is at constant temperature T_i in its central part ($|z| \leqslant r_o/2$), and the radial heat flux vanishes ($\partial T(s_i)/\partial s = 0$) for $r_o/2 \leqslant |z| \leqslant r_o$. The value of the imposed magnetic field decreases as the inverse of s in the bulk of the fluid and is zero outside as described in § 2.1.

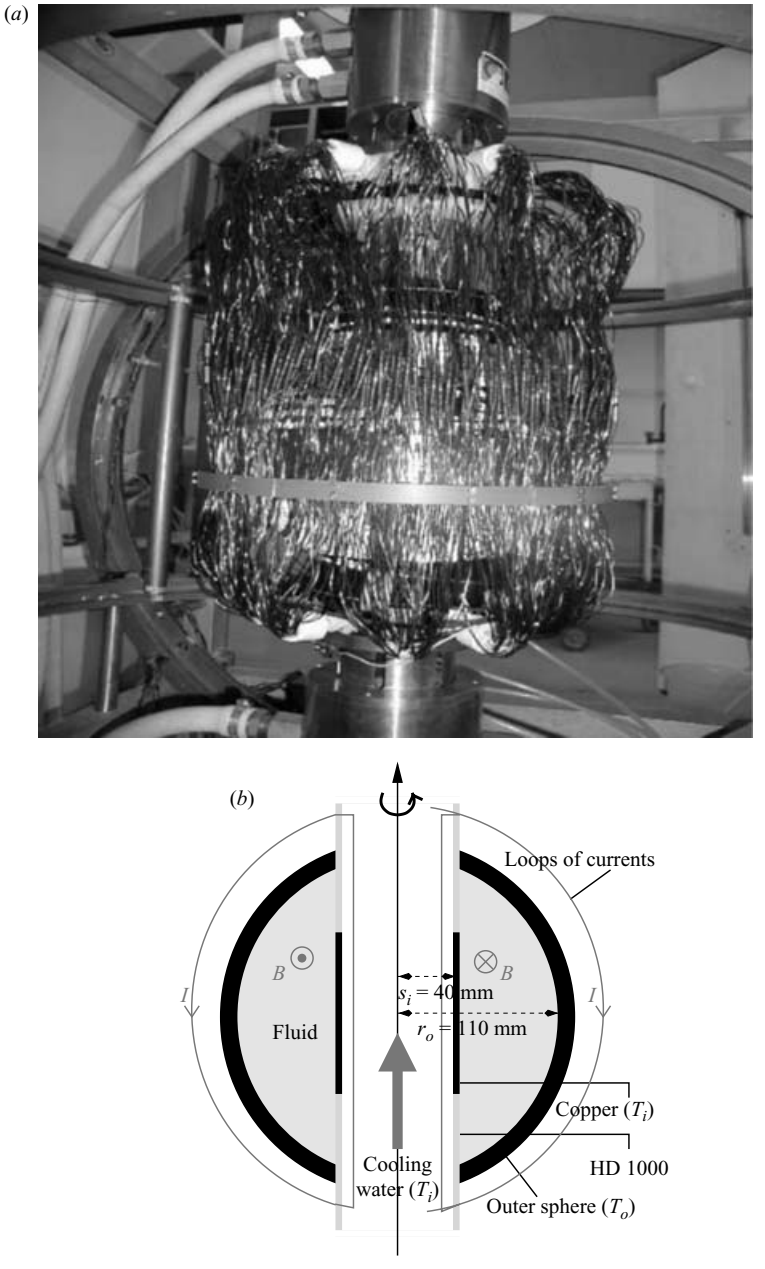

FIGURE 1. (*a*) Picture of the apparatus used in magnetoconvection experiments. The solenoid that partly hides the sphere is built from a copper wire that loops in and out of the inner cylinder and the outer sphere. (*b*) Meridional cross-section of the co-rotating sphere and inner cylinder. The imposed z-invariant toroidal magnetic field is generated by the longitudinal distribution of current I in a solenoidal electrical coil.

The continuity, momentum and heat equations are, in dimensionless form,

$$\nabla \cdot \boldsymbol{u} = 0, \tag{2.1}$$

$$\frac{\mathrm{d}\boldsymbol{u}}{\mathrm{d}t} + \frac{2}{E}\,\hat{\boldsymbol{z}} \times \boldsymbol{u} = -\nabla \Pi - \frac{R}{P}(T - T_{\mathrm{ref}})s\,\hat{\boldsymbol{s}} + \nabla^2 \boldsymbol{u} + \frac{\Lambda}{E}\boldsymbol{j} \times \boldsymbol{B}, \tag{2.2}$$

Definition	Expression	Gallium experiments	Earth's core
P, Prandtl	ν/κ	$0.022 - 0.025$	$\sim 10^{-1}$
E, Ekman	$\nu/\Omega d^2$	$9.7\times10^{-7} - 2.9\times10^{-6}$	$\sim 10^{-15}$
E_κ, thermal Ekman	$\kappa/\Omega d^2$	$3.9\times10^{-5} - 1.2\times10^{-4}$	$\sim 10^{-14}$
E^*, modified Ekman	$(\kappa+\nu)/\Omega d^2$	$3.9\times10^{-5} - 1.2\times10^{-4}$	$\sim 10^{-14}$
R, Rayleigh	$\alpha\Delta T\Omega^2 d^4/\kappa\nu$	$8.6\times10^{6} - 8.4\times10^{7}$	–
P_m, magnetic Prandtl	ν/λ	1.4×10^{-6}	$\sim 10^{-6}$
Λ, Elsasser	$\sigma\mathscr{B}^2/\rho\Omega$	$< 10^{-2}$	~ 1

TABLE 2. Values of the dimensionless parameters in the gallium experiment and in the Earth's core. Numbers are calculated from the physical properties listed in table 1. We use for the Earth's core $d = 2.3\times10^6$ m, $\Omega = 7.27\times10^{-5}$ rad s^{-1} and $\mathscr{B}\sim10^{-3}$ T. The Rayleigh number of the Earth's core is not computed since only the superadiabatic part of ΔT is relevant.

$$\frac{\mathrm{d}\Theta}{\mathrm{d}t} + \boldsymbol{u}\cdot\nabla T^{\mathrm{ic}}_{\mathrm{cond}} = P^{-1}\nabla^2\Theta, \tag{2.3}$$

where $\boldsymbol{u}$ is the velocity field, Π is the modified pressure, T is the temperature of the fluid, T_{ref} is a reference temperature, $T^{\mathrm{ic}}_{\mathrm{cond}}$ is the temperature conductive profile which satisfies the boundary conditions described above (the superscript 'ic' stands for an inner cylinder), $\Theta = T - T^{\mathrm{ic}}_{\mathrm{cond}}$ is the temperature perturbation, $\boldsymbol{j}$ is the electrical current density and $\boldsymbol{B}$ is the magnetic field. The dimensionless numbers in the set of equations ((2.1), (2.2), (2.3)) are defined in table 2. These equations have been made non-dimensional using $\Delta T = T_o - T_i$ as the unit of temperature, the gap $d = r_o - s_i$ as the unit of length, and the viscous diffusive time d^2/ν as the unit of time. The unit of the magnetic field is $\mathscr{B}$, the intensity of the imposed magnetic field at $s^* = 1.25\ s_i$ (corresponding to a cylindrical radius of 50 mm in the experiment where $s_i = 40$ mm and $r_o = 110$ mm), where convection is the most active. The electrical density currents unit is $\sigma\nu\mathscr{B}/d$, so that the unit of electrical potential is $\nu\mathscr{B}$. From now on in the paper, r_0, s_i, T_o and T_i are non-dimensional.

2.3. *Quasi-geostrophic flow/three-dimensional magnetic induction numerical model*

In this section we incorporate the effect of magnetic forces into the two-dimensional quasi-geostrophic model derived in Part 1. We then obtain a mixed quasi-geostrophic flow/three-dimensional magnetic induction model of rapidly rotating magnetoconvection. We need to introduce the Lorentz force term, the last term on the right-hand side of equation (2.2), in the quasi-geostrophic approximation of the momentum equation. We denote by $\mathscr{U}$, ℓ and b respectively the typical velocity amplitude, length scale and induced magnetic field intensity. The magnetic Reynolds number $R_m = \mathscr{U}\ell/\lambda$ is small in our experiments and $b/\mathscr{B} \simeq O(R_m) < 10^{-3}$. As we prescribe a current-free magnetic field, electrical currents are associated with the induced field $\boldsymbol{b}$ only, through Ampère's law

$$\nabla\times\boldsymbol{b} = P_m\boldsymbol{j}. \tag{2.4}$$

We impose non-penetration boundary conditions on the electrical currents

$$\boldsymbol{j}\cdot\boldsymbol{n} = 0. \tag{2.5}$$

Thus we do not follow Busse & Finocchi (1993) or Petry, Busse & Finocchi (1997), who noted that in the case of perfectly conducting boundaries the induced field $\boldsymbol{b}$

is z-invariant. We need here to describe the induced electrical currents in the entire volume between the inner cylinder and the outer sphere. As $R_m \ll 1$, the electrical field is irrotational and Ohm's law is

$$\boldsymbol{j} = -\nabla V + \boldsymbol{u} \times \boldsymbol{B}, \tag{2.6}$$

with V the electric potential. In this diffusive regime, the Elsasser number Λ is the appropriate parameter to compare the magnetic force to the rotation force. It remains small ($\Lambda \leqslant 10^{-2}$, see table 2). Thus, as in Part 1, we base our numerical model on the quasi-geostrophic approximation. As the Elsasser number is small, boundary layers are of the Ekman type. Joule heating is neglected (like the viscous heating in the Boussinesq approximation) and the heat equation in our quasi-geostrophic flow/three-dimensional magnetic induction model remains identical to equation (3.12) in Part 1. The Joule heating scales as $\sigma d^3 \mathscr{U}^2 \mathscr{B}^2$, which is of the order of 10^{-5} W for $\mathscr{U} = 10^{-2}\,\mathrm{m\,s^{-1}}$. It is negligible in comparison to the total heat flux, of the order of 10^2 W.

Since the imposed magnetic field is toroidal, it has no direct influence on the zonal motions. Thus the Lorentz force does not appear in the equation for the zonal wind, which remains identical to equation (3.11) in Part 1. Therefore, the only modification we introduce to turn the convection model of Part 1 into a magnetoconvection model is the introduction, on the right-hand side of the z-integrated vorticity equation (3.10) in Part 1, of the term

$$\frac{\Lambda}{E}\langle \nabla \times [\boldsymbol{j} \times \boldsymbol{B}] \cdot \hat{\boldsymbol{z}} \rangle_z \tag{2.7}$$

due to the Lorentz force. Given the geometry of the imposed field (see § 2.1), we write expression (2.7) as

$$-\frac{\Lambda}{E}\frac{s^*}{s^2}\left\langle \frac{\partial j_z}{\partial \phi} \right\rangle_z = -\frac{\Lambda}{E}\frac{s^*}{s^2}\frac{\partial}{\partial \phi}\left[\frac{s^* \widetilde{u}_s}{s} - \frac{[V]_{-H}^{+H}}{2H} \right], \tag{2.8}$$

with $H = \sqrt{r_o^2 - s^2}$ the half-height of the fluid column. We denote here by $\widetilde{\boldsymbol{u}}$ the non-axisymmetric flow, so that $\boldsymbol{u} = \widetilde{\boldsymbol{u}} + \overline{\boldsymbol{u}} = \widetilde{u}_s(s, \phi, t)\,\hat{\boldsymbol{s}} + [\overline{u}_\phi(s, t) + \widetilde{u}_\phi(s, \phi, t)]\hat{\boldsymbol{\phi}}$ since the axisymmetric radial flow vanishes in the quasi-geostrophic representation. We consider in the quasi-geostrophic approximation that u_z is linear in the z-direction (Gillet & Jones 2006). Then taking the divergence of (2.6) we obtain the following equation for V in the bulk of the fluid:

$$\Delta V = \frac{s^*}{s} z \frac{\partial}{\partial s}\left(\frac{\eta \widetilde{u}_s}{H} \right). \tag{2.9}$$

We note that the quasi-geostrophic approximation requires that both the Rossby number $Ro = \mathscr{U}/\Omega \ell$ and the Elsasser number Λ are small. The slope $\eta = -\mathrm{d}H/\mathrm{d}s = s/H$ of the container boundary with respect to a plane perpendicular to the rotation axis is also assumed to be small, $\eta \ll 1$, in order to derive the quasi-geostrophic equations. It would be consistent with these assumptions to neglect terms that are $O(\Lambda\eta)$ in the quasi-geostrophic momentum equation whilst the Coriolis term is $O(\eta)$, the inertial term is $O(Ro)$ and the main magnetic term is $O(\Lambda)$. As we use the quasi-geostrophic model for $O(1)$ values of η, we have chosen to keep these $O(\Lambda\eta)$ terms that are required if the boundary condition (2.5) is to be satisfied.

The electric potential V in (2.9) is described with a finite difference decomposition in the $(\hat{\boldsymbol{r}}, \hat{\boldsymbol{\theta}})$-plane and, like ψ and $\langle \Theta \rangle_z$, with a spectral decomposition in the $\hat{\boldsymbol{\phi}}$-direction.

It is antisymmetric with respect to the equatorial plane. Equation (2.9) is therefore solved with a successive over-relaxation method (SOR) in the upper part of the fluid cavity only. At each time step the value of V, calculated from the velocity field, is introduced in the term associated with the Lorentz force and given in equation (2.8). Finally, we obtain a quasi-geostrophic flow/three-dimensional magnetic induction model in which the motions are described with a quasi-geostrophic approach whereas the induced electrical currents are computed in the entire volume. An example of an electrical potential distribution with the associated electrical currents is presented in figure 2. As in the study of a geostrophic vortex in a transverse magnetic field by Brito *et al.* (1995), the electrical currents $\boldsymbol{j} \simeq \boldsymbol{u} \times \boldsymbol{B}$ are nearly vertical: the currents go up on one side of the vortices, and down on the other side. Near the boundary of the container, electrical potential gradients ensure that the electrical currents are deflected from the insulator (see equation (2.5)).

We evaluate now the magnitude of the non-axisymmetric radial motions as $\widetilde{U}_s = \max\{\widetilde{U}_{\mathrm{rad}}(s)\}$, and the magnitude of the axisymmetric azimuthal flow as $\overline{U} = \max\{-\overline{U}_{\mathrm{zon}}(s)\}$. These can be computed from both our ultrasonic Doppler velocimetry measurements and the numerical model. The magnitude of the non-axisymmetric azimuthal motions is only accessible numerically. To be consistent with what can be done experimentally (see § 2.1), it is evaluated as $\widetilde{U}_\phi = \max\{\widetilde{U}_{\mathrm{azi}}(s)\}$, where $\widetilde{U}_{\mathrm{azi}}(s) = (\langle[\widetilde{u}_\phi - \langle\widetilde{u}_\phi\rangle_\tau]^2\rangle_\tau)^{1/2}$.

3. Onset of rapidly rotating spherical convection in the presence of an imposed azimuthal magnetic field

Fearn (1979*b*) and Soward (1979) have developed a local asymptotic theory of convection in a rotating sphere permeated by a magnetic field. They have found that adding an azimuthal magnetic field delays the onset of convection as long as

$$\Lambda < O\left(\eta^{2/3} E_\kappa^{1/3}\right). \tag{3.1}$$

In this regime, the frequency ω_c of the critical mode decreases as Λ increases. The critical mode is a modified thermal Rossby wave that propagates in the prograde direction. For higher values of Λ, while the pulsation still decreases, inertial and viscous processes become negligible and the magnetic field has a destabilizing effect, convection appearing for a lower R as compared to the rotating case without magnetic field.

We now discuss the onset of magnetoconvection as predicted from our computations based on the quasi-geostrophic approximation of the momentum equation and a fully three-dimensional model of the induction effects. We compare our results with the local asymptotic theory and with the conclusions of Petry *et al.* (1997), who studied magnetoconvection in an annulus with inclined, perfectly conducting boundaries and stress-free conditions for the velocity. Figure 3 illustrates how the critical parameters depend on the Elsasser number. A maximum of R_c is found close to $\Lambda = E_\kappa^{1/3}$, as expected from the asymptotic analysis. Both the wavenumber and the pulsation at onset of magnetoconvection decrease when the Elsasser number increases. There is a progressive transition from a modified thermal Rossby mode to a magnetic mode (a Rossby wave driven by buoyancy against magnetic diffusion instead of thermal diffusion).

Figure 4 gives examples of the vorticity structure at the onset of convection and magnetoconvection. The azimuthal size of the convective cells increases as a function of the imposed magnetic field. In Part 1 we had implicitly considered equal radial

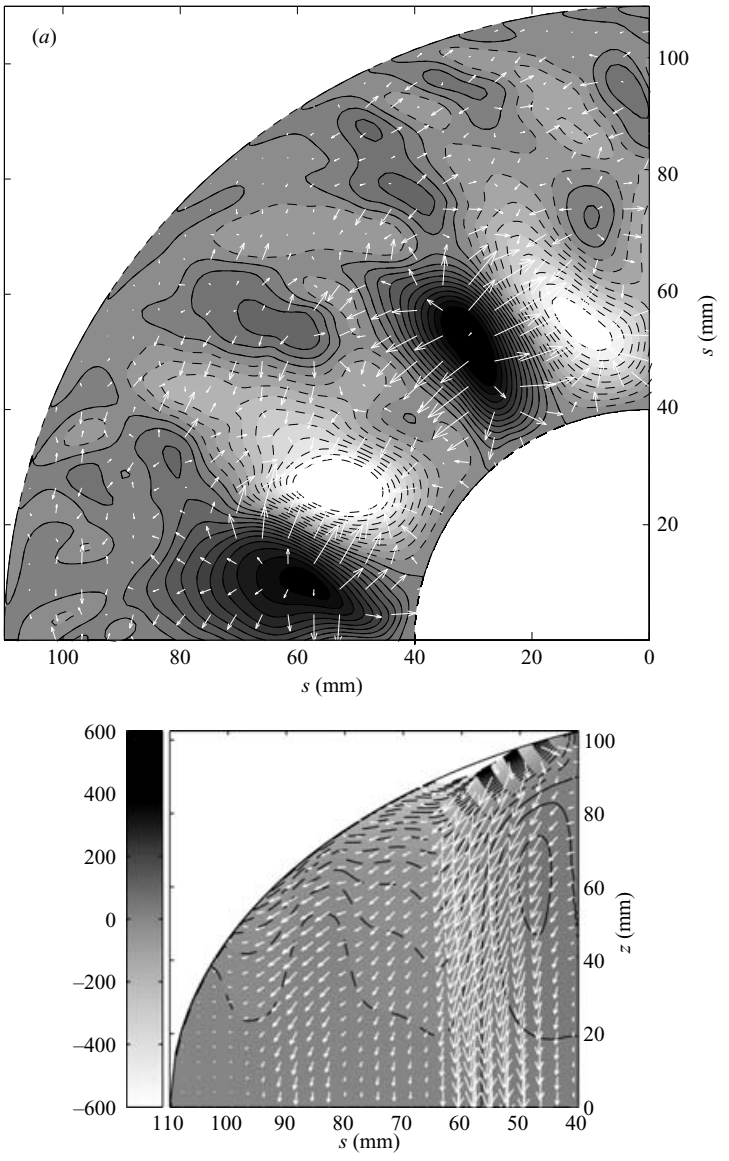

FIGURE 2. Snapshot of the spatial distribution of dimensionless electrical potentials and associated electrical currents (white arrows), for $P = 0.025$, $E = 1.95 \times 10^{-6}$, $\Lambda = 3.9 \times 10^{-2}$ and $R = 5\ R_c$. (*a*) The top outer boundary (viewed from above), (*b*) meridional cross-section in the plane indicated by the dashed line in (*a*). The colour scale in (*a*) is the same as in (*b*). Positive (resp. negative) isocontours are represented by solid (resp. dashed) lines. A dimensionless potential of 600 corresponds to approximately $8\mu V$.

and azimuthal length scales of the vortices. Here the Lorentz forces associated with a toroidal magnetic field tend to oppose radial motions (omitting the effect of electrically insulating boundaries, $\boldsymbol{j} \times \boldsymbol{B} \propto -B^2 \widetilde{u}_s \hat{\boldsymbol{s}}$). At onset azimuthal motions $\widetilde{u}_\phi$ are therefore favoured over the radial ones $\widetilde{u}_s$. From the continuity equation, the geostrophic flow

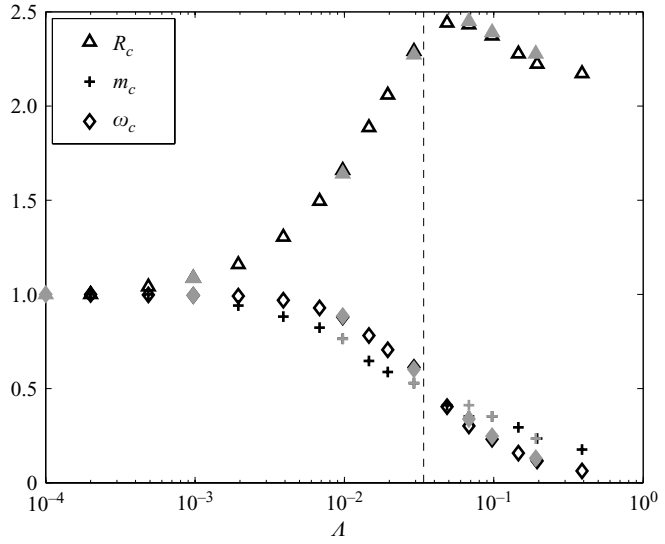

FIGURE 3. Evolution of the critical parameters for magnetoconvection, determined from our numerical computations: R_c, m_c and ω_c (normalized to the non-magnetic case) as a function of Λ, for $E = 9.74 \times 10^{-7}$ and $P = 0.025$. The grey symbols (respectively black) are from calculations with (respectively without) the computation of the electrical potential V. The dashed line is given by $\Lambda = E_\kappa^{1/3}$.

satisfies $\partial(s\widetilde{u}_s)/\partial s + \partial\widetilde{u}_\phi/\partial\phi = 0$, so that

$$\frac{\widetilde{U}_s}{\ell_s} \sim \frac{\widetilde{U}_\phi}{\ell_\phi}. \tag{3.2}$$

We denote by ℓ_s and ℓ_ϕ the typical length scales of the vortices in the radial and azimuthal directions respectively. As a consequence of the toroidal magnetic field, the ratio ℓ_s/ℓ_ϕ must decrease with Λ. Added to the β-effect due to rapid rotation together with a varying height $H(s)$ (see Part 1), a second source of anisotropy is induced in our system by the presence of a magnetic field.

The influence of the electrical boundary conditions on the critical values is evaluated by comparison of a linear analysis with and without the computation of the electrical potential V term in equation (2.8). The difference (see figure 3) remains negligible in the weak-field case whereas a small stabilizing effect of insulating boundaries is found for $\Lambda > E_\kappa^{1/3}$ (in contrast to the plane layer case (Aurnou & Olson 2001) for which the numerical analysis of Zhang, Weels & Roberts (2004) indicates a strong destabilizing effect of insulating boundaries). We note that this is consistent with the quasi-geostrophic approximation approach that taking into account the $O(\Lambda\eta)$ potential term in equation (2.9) does not significantly affect the results. Our results – e.g. a destabilizing effect of the magnetic field, in a limited range of Λ, at the experimental values of Ekman and Prandtl numbers – are consistent with the conclusions of Petry *et al.* (1997), despite the specific details of their model. We thus validate their more systematic exploration of the parameter space (with variable direction of the imposed field).

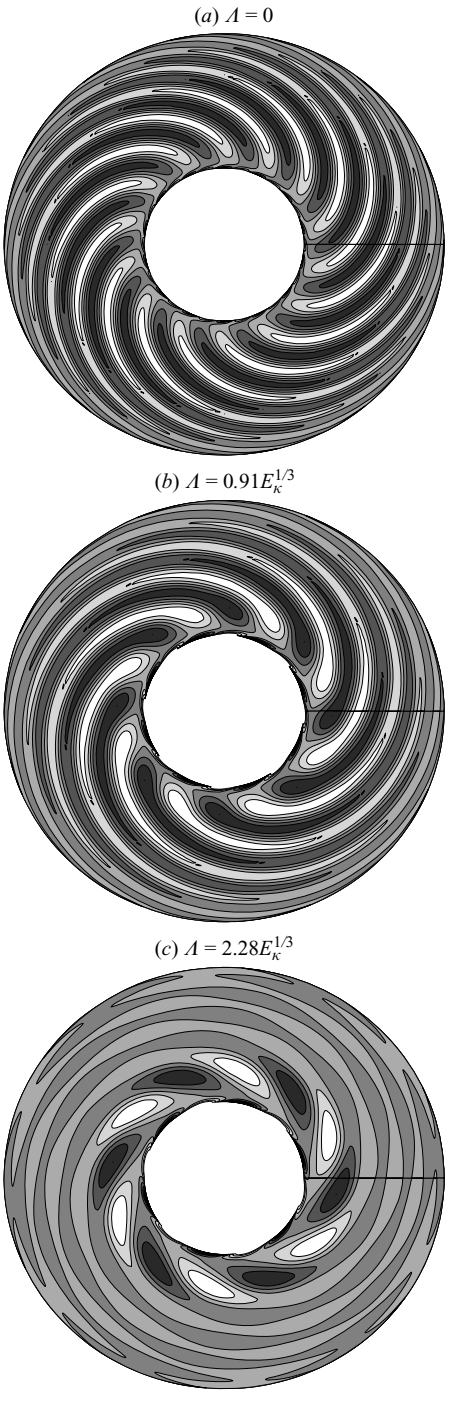

FIGURE 4. Snapshots of convection and magnetoconvection at the onset, obtained from the quasi-geostrophic flow/three-dimensional magnetic induction: normalized vorticity maps in the equatorial plane, for $P = 0.025$, $E = 1.95 \times 10^{-6}$, and different values of Λ.

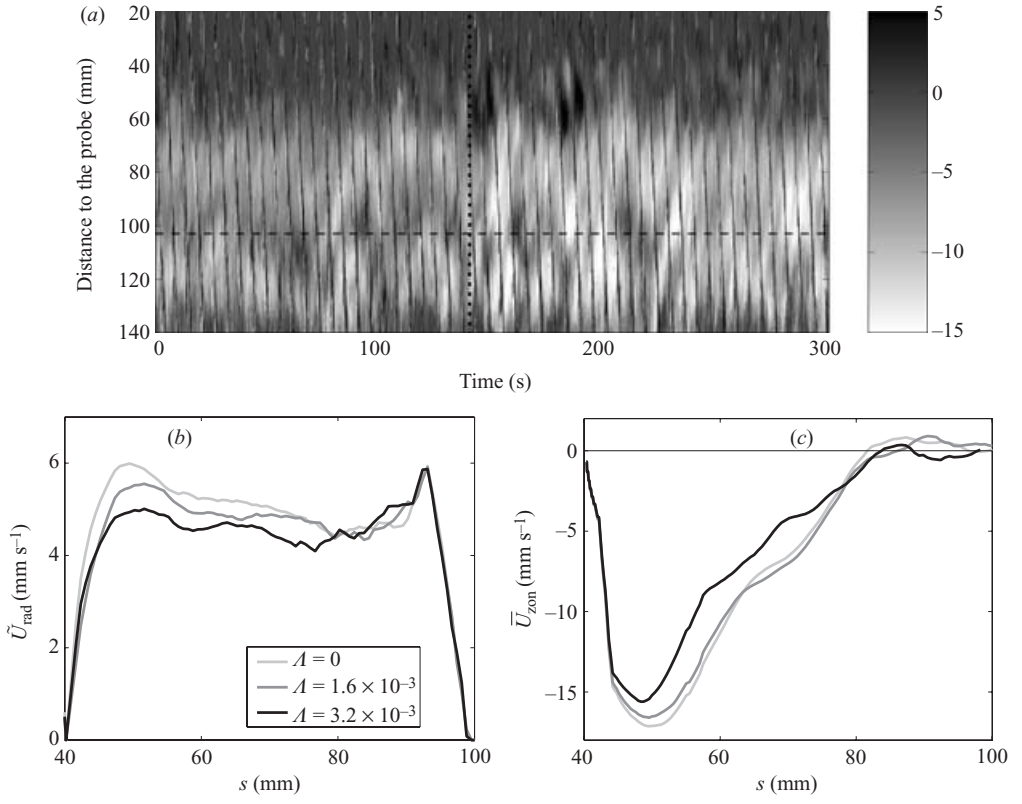

FIGURE 5. Ultrasonic Doppler velocimetry measurements performed during magnetoconvection experiments. (a) Transverse velocity profiles $u_\chi(s,t)$ in mm s^{-1}, as a function of time and distance from the probe, with $P = 0.025$, $E = 1.95 \times 10^{-6}$ and $R = 1.74 \times 10^7$. The vertical dashed line near 140 s corresponds to the transition from $\Lambda = 3.6 \times 10^{-3}$ ($R = 2.2\ R_c$) to $\Lambda = 0$ ($R = 2.6\ R_c$). The horizontal dashed line indicates the distance at which the transverse beam line is the closest to the tangent cylinder (see figure 2, Part 1). The tilted black lines are an artifact due to the electromagnetic noise. (b) R.m.s. radial velocity profiles $\widetilde{U}_{\rm rad}(s)$ for $E = 9.74 \times 10^{-7}$. $R = 7.93 \times 10^7$ is kept constant and Λ varies. (c) Zonal velocity profiles $\overline{U}_{\rm zon}(s)$ for $E = 9.74 \times 10^{-7}$. $R = 6.06 \times 10^7$ is kept constant and Λ varies.

4. Nonlinear rapidly rotating spherical convection in presence of an imposed azimuthal magnetic field

Following the studies by Or & Busse (1987) and Schnaubelt & Busse (1992) for $\Lambda = 0$, the magnetoconvection analysis of Petry *et al.* (1997) included the nonlinear regime close to onset. They focused on the zonal wind generation just above onset and concluded that imposing a zonal magnetic field does not significantly alter the evolution of either the zonal flow or the heat flux as a function of the Rayleigh number. As in the non-magnetic case presented in Part 1, we study here the nonlinear regime for $R/R_c < 6$, but in the presence of an imposed toroidal magnetic field.

4.1. *Impact of the magnetic field on the flow*

For a given value of the Rayleigh number in the experiments, changes in the amplitude of convective motions are observed as a function of Λ. As an example in figure 5(a) the zonal velocity abruptly becomes stronger when we switch off the magnetic field. The changes in the velocity profiles $\widetilde{U}_{\rm rad}$ and $\overline{U}_{\rm zon}$ are illustrated in figure 5(b,c). The

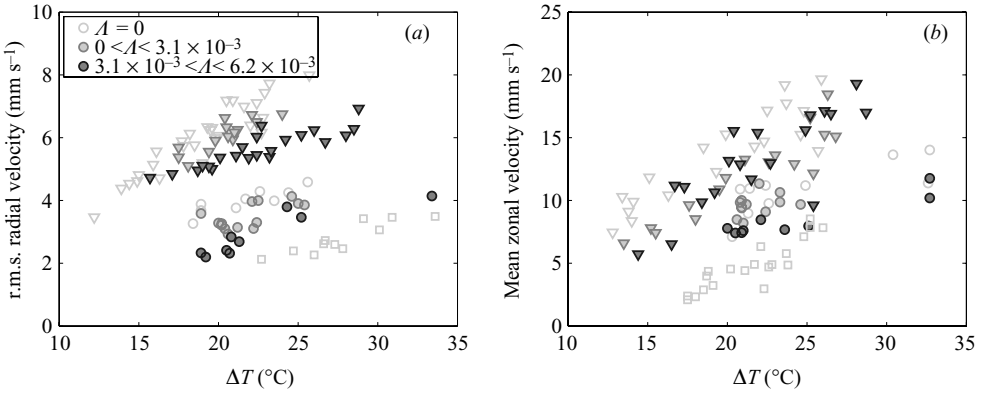

FIGURE 6. Comparison of velocity measurements between convection and magnetoconvection experiments: (*a*) r.m.s. radial velocity $\widetilde{U}_s$ (in mm s^{-1}) and (*b*) mean zonal velocity $\overline{U}$ (in mm s^{-1}) as a function of ΔT (in°C), for $P = 0.025$, $E = 2.92 \times 10^{-6}$ (squares), $E = 1.95 \times 10^{-6}$ (circles), $E = 9.74 \times 10^{-7}$ (triangles) and different Λ. The different greys giving the value of Λ for $E = 1.95 \times 10^{-6}$ are similarly used for $E = 2.92 \times 10^{-6}$ and $E = 9.74 \times 10^{-7}$.

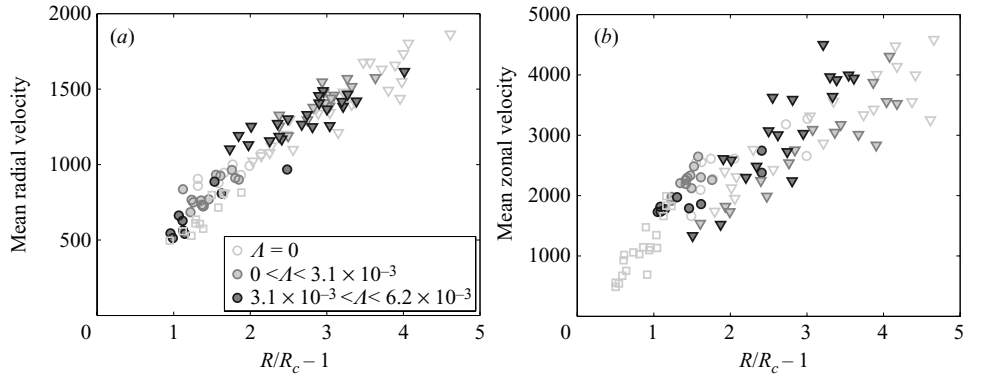

FIGURE 7. Comparison of velocity measurements between convection and magnetoconvection experiments: (*a*) r.m.s. radial velocity $\widetilde{U}_s$ and (*b*) mean zonal velocity $\overline{U}$ as a function of $(R/R_c - 1)$, for $P = 0.025$, $E = 2.92 \times 10^{-6}$ (squares), $E = 1.95 \times 10^{-6}$ (circles), $E = 9.74 \times 10^{-7}$ (triangles) and different Λ. The different greys giving the value of Λ for $E = 1.95 \times 10^{-6}$ are similarly used for $E = 2.92 \times 10^{-6}$ and $E = 9.74 \times 10^{-7}$.

magnetic versus non-magnetic experiments – with the other parameters E and R kept fixed – show differences up to 25% in amplitude of convective and zonal velocities, as illustrated in figure 6(*a, b*), which presents $\overline{U}$ and $\widetilde{U}_s$ as a function of ΔT.

In the case of the non-magnetic rotating convection, the amplitude of the convective motions scales at first order with $(R - R_c)$. In rotating magnetoconvection, $(R - R_c)$ decreases as Λ is increased from 0 to $E_\kappa^{1/3}$ due to the stabilizing effect of the magnetic field (see § 3). In the range of parameters covered by our experiments, the modification of the onset of convection indeed suffices to explain the variation of the amplitude of measured rms radial velocities $\widetilde{U}_s$, as seen in figure 7(*a*). We have unfortunately not been able to exceed experimentally the $\Lambda = E_\kappa^{1/3}$ limit, and thus have not been able to explore the destabilizing effect of the magnetic field. Figure 7(*b*) presents all our mean measurements of the zonal flow. The increase of R_c with Λ explains part of the decrease in $\overline{U}$ at constant R. However at R/R_c constant instead, a slight increase

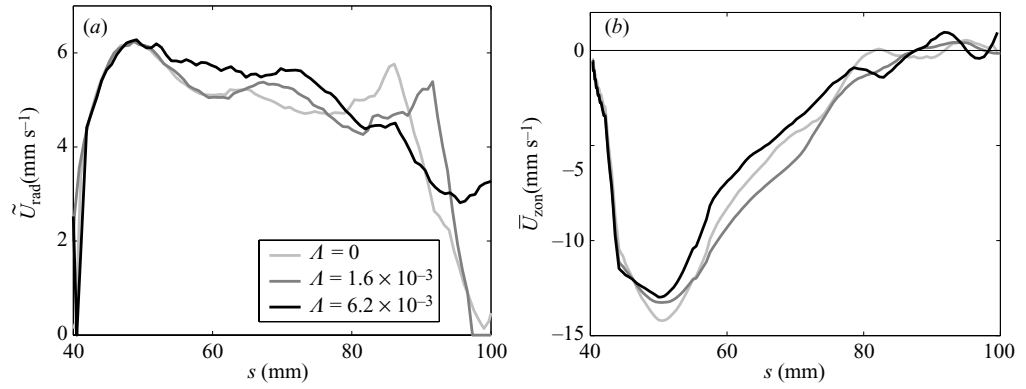

FIGURE 8. Velocity measurements during magnetoconvection experiments for $E = 9.74 \times 10^{-7}$, R/R_c being kept constant and Λ varying: (a) r.m.s. radial velocity profiles $\widetilde{U}_{\rm rad}(s)$ at $R/R_c = 4.2$ and (b) zonal velocity profiles $\overline{U}_{\rm zon}(s)$ at $R/R_c = 4$.

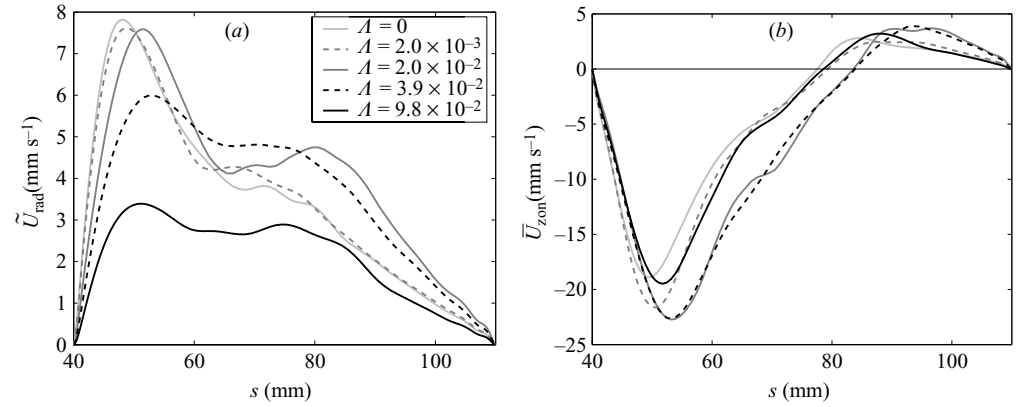

FIGURE 9. Quasi-geostrophic flow – three-dimensional magnetic induction numerical reconstruction of velocity profiles for magnetoconvection: (a) r.m.s. radial velocity profiles $\widetilde{U}_{\rm rad}(s)$ and (b) zonal velocity profiles $\overline{U}_{\rm zon}(s)$, for $E = 1.95 \times 10^{-6}$, $R/R_c = 3$ and $\Lambda/E_\kappa^{1/3} = 0, 0.05, 0.45, 0.9$ and 2.88 respectively.

of $\overline{U}$ with Λ may be detected, in particular in the experiments at $E = 9.74 \times 10^{-7}$. Nevertheless the dispersion of the data points makes it difficult to draw conclusions.

Figure 8(a) presents several profiles of $\widetilde{U}_{\rm rad}(s)$ for a given value of $R/R_c = 4.2$ and varying Λ. At first order we verify that all the profiles have similar amplitude. At second order we detect a slight enlargement of the convective area as the magnetic field becomes closer to $E_\kappa^{1/3}$. That would suggest that the organization of the convection is modified when $E_\kappa^{1/3}$ is approached, as will be detailed in § 4.3 with the help of our computations. Similarly, no clear modification has been detected in the mean zonal profiles as a function of Λ in figure 8(b), where $R/R_c = 4$.

4.2. *Comparison with the quasi-geostrophic flow/three-dimensional magnetic induction simulations*

We present in figure 9 typical radial profiles $\widetilde{U}_{\rm rad}$ and zonal profiles $\overline{U}_{\rm zon}$ for several intensities of the imposed field (E and R/R_c kept constant), from quasi-geostrophic flow/three-dimensional magnetic induction simulations. Approaching the

$\Lambda/E_\kappa^{1/3}$	0	0.05	0.45	0.90	2.88
$\widetilde{U}_s$	945	949	1051	970	556
$\widetilde{U}_\phi$	996	1036	1124	1153	929
$\overline{U}$	1815	2072	2496	2509	1954
$\widetilde{U}_s/\widetilde{U}_\phi$	0.95	0.92	0.93	0.84	0.60

TABLE 3. Quasi-geostrophic flow/three-dimensional magnetic induction simulation of the r.m.s. radial velocity U_s, the r.m.s. azimuthal velocity $\widetilde{U}_\phi$, the mean zonal velocity $\overline{U}$ and the ratio $\widetilde{U}_s/\widetilde{U}_\phi$, for $P=0.025$, $E=1.95\times10^{-6}$, $R/R_c=3$ and several values of the Elsasser number, respectively $\Lambda=0,\ 2.1\times10^{-3},\ 1.9\times10^{-2},\ 3.8\times10^{-2}$ and 1.2×10^{-1}.

limit $\Lambda\simeq E_\kappa^{1/3}$, we notice the emergence of a second maximum in $\widetilde{U}_{\rm rad}$ (figure 9*a*). Meanwhile, the maximum of $\widetilde{U}_{\rm rad}$ migrates slightly towards larger radii, although its amplitude remains constant. These characteristics are qualitatively in agreement with the experimental radial measurements at the highest Λ (figure 8*a*). A displacement of the minimum of the numerical zonal profiles towards the outer boundary is also observed in figure 8(*b*). In these zonal profiles, the shape modification is accompanied by an increase of the amplitude $\overline{U}$. This suggests that the tendency observed in our experimental measurements of $\overline{U}$ (figure 7*b*) may be significant. Figure 9 also presents velocity profiles for Λ larger than $E_\kappa^{1/3}$. It appears that the convection intensity drops severely once convection starts from magnetic modes, with a decrease in both velocities $\widetilde{U}_s$ and $\overline{U}$. The r.m.s. radial profiles also become increasingly flat, suggesting that convection becomes relatively easier at larger radius, where the magnetic field is weaker.

Figure 10 shows several numerical vorticity maps obtained with the quasi-geostrophic simulations, illustrating convection patterns for Elsasser numbers both lower and higher than $E_\kappa^{1/3}$ (the ratio $R/R_c=3$ is kept constant). It shows that vorticity isolines elongate along the magnetic field direction, in a way similar to what we first noticed at onset (figure 4). This anisotropy in the vortices (ℓ_ϕ/ℓ_s increases with Λ) is associated with a relative increase of the typical r.m.s. azimuthal motions $\widetilde{U}_\phi$ compared to the r.m.s. radial motions $\widetilde{U}_s$. This point is illustrated in table 3 where we see that $\widetilde{U}_s$ is much more affected than $\widetilde{U}_\phi$ by the transition across $E_\kappa^{1/3}$.

We also detect in figure 10 that convection intensifies at larger radius, where the intensity of the magnetic field is weaker, as Λ is increased. This observation is correlated with the modifications in $\widetilde{U}_{\rm rad}$ (shift of the maximum, and profiles more flat) noticed in figure 9(*a*) as Λ exceeds $E_\kappa^{1/3}$. We reach a maximum value of $\Lambda\simeq0.2\ E_\kappa^{1/3}$ in our experiments at $E=9.74\times10^{-7}$ (the best documented case). In the range of Elsasser number available experimentally, our numerical simulations indicate an evolution of the critical wavenumber m_c, from 17 in the non-magnetic case down to 14 (see figure 3). We could expect an increase of both ℓ_ϕ/ℓ_s and $\widetilde{U}_\phi/\widetilde{U}_s$. The ultrasonic Doppler velocimetry measurements in our set-up are unfortunately not precise enough to detect such a tiny modification in the azimuthal wavenumbers, and a direct measurement of the r.m.s. azimuthal velocity $\widetilde{u}_\phi$ was not available.

4.3. *Impact of the magnetic field on the inertial scaling*

The change in geometry of the vortices as we increase Λ (see figure 10) should induce a deviation from the scaling law (1.2) obtained for $\overline{U}$ in the non-magnetic case. The

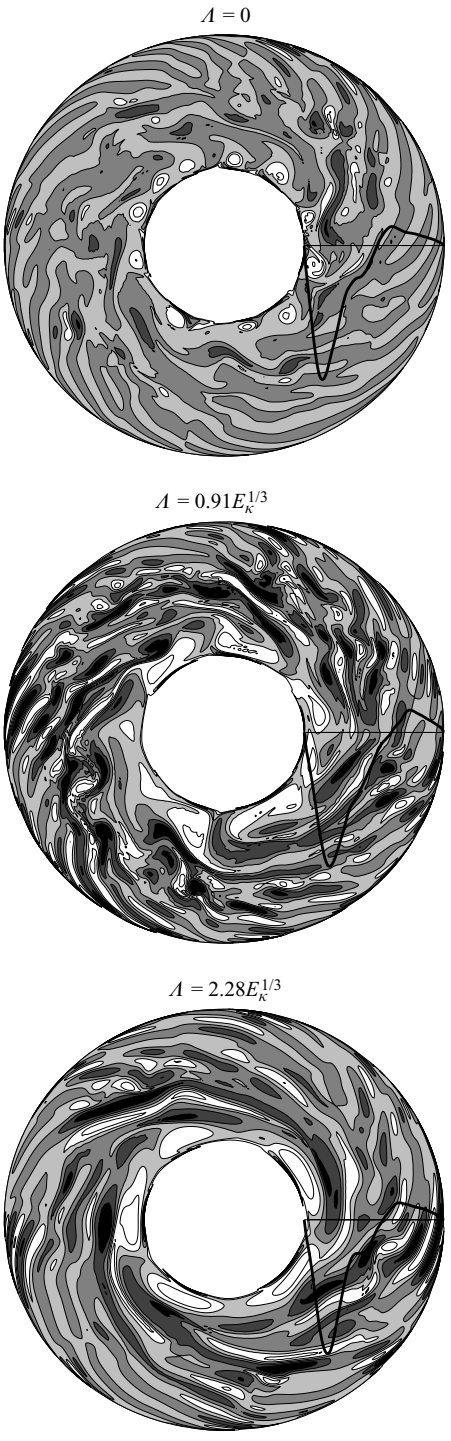

FIGURE 10. Snapshots of convection and magnetoconvection obtained from numerical simulation: normalized vorticity maps in the equatorial plane, for $P = 0.025$, $E = 1.95 \times 10^{-6}$, $R = 3\ R_c$ and different values of Λ. The colour scale is from -0.1 (white) to $+0.1$ (black). Superimposed on the vortices, the mean zonal flow is drawn with a black solid line as a function of radius.

equation for the mean zonal flow (equation (3.11), Part 1) can be written

$$\frac{\partial \overline{u}_\phi}{\partial t} + \overline{\widetilde{u}_s \frac{\partial \widetilde{u}_\phi}{\partial s}} = \frac{\partial}{\partial s}\left[\frac{1}{s}\frac{\partial}{\partial s}\left(s\overline{u}_\phi\right)\right] - \sqrt{\frac{r_o\beta(s)}{2sH}}\overline{u}_\phi. \tag{4.1}$$

If Ekman friction balances the nonlinear term on the left-hand side of equation (4.1), as in the convection case for $P \ll 1$, we obtain the estimation

$$\sqrt{\frac{r_o\beta(s)}{2sH}}\overline{U} \sim \frac{\widetilde{U}_s\widetilde{U}_\phi}{\ell_s}. \tag{4.2}$$

The Rhines length scale which results from a balance between the Coriolis and inertial forces in the vorticity equation (equation (3.8), Part 1), provides the radial extent ℓ_β of the zonal jets. In the present case where the flow is dominated by its axisymmetric part, ℓ_β is equivalent to the radial length ℓ_s of the vortices, as illustrated in the vorticity maps in figure 10. Substituting ℓ_s in equation (4.2) by ℓ_β from equation (1.1) leads to

$$\sqrt{\frac{r_o\beta(s)}{2sH}}\overline{U} \sim \sqrt{\frac{\beta(s)}{\overline{U}}}\widetilde{U}_s\widetilde{U}_\phi, \tag{4.3}$$

and finally

$$\left(\frac{r_o}{2sH}\right)^{1/3}\overline{U} \sim \left(\widetilde{U}_s\widetilde{U}_\phi\right)^{2/3} \tag{4.4}$$

(to be compared with equation (4.6) in Part 1). As already noticed in Part 1 the prefactor on the left-hand side is almost constant throughout the main part of the liquid volume (except in the region very close to the equator). Using the estimation (3.2) from the continuity equation, equation (4.4) leads to

$$\overline{U} \sim \left(\widetilde{U}_s\widetilde{U}_\phi\right)^{2/3} \sim \widetilde{U}_s^{4/3}\left(\frac{\ell_\phi}{\ell_\beta}\right)^{2/3}, \tag{4.5}$$

which extends equation (4.7) of Part 1 to cases where anisotropy is present.

This scaling law (4.5) is *a priori* valid in any anisotropic system where ℓ_β differs from ℓ_ϕ, like for example in the frame of β-plane turbulence (e.g. Galperin *et al.* 2004; Read *et al.* 2004). As we have barely detected this effect in our non-magnetic study (see figure 13, Part 1), we have kept a simpler description with $\ell_\beta = \ell_\phi$ in Part 1; in more turbulent fluid flows than those considered in Part 1, the scaling law (4.5) might however be relevant even without the presence of a magnetic field. In our present study, the imposed magnetic field appears to constrain ℓ_ϕ much more than any non-magnetic effect.

The scaling (4.5) is tested numerically in figure 11(*a*), where $\overline{U}$ is represented as a function of $\sqrt{\widetilde{U}_s\widetilde{U}_\phi}$ for several Ekman and Elsasser numbers (we do not present $\overline{U}$ as a function of $\widetilde{U}_s\sqrt{\ell_\phi/\ell_\beta}$ because it is difficult numerically to precisely determine ℓ_ϕ and ℓ_β). For $\Lambda = 0$ the 4/3 law is verified for several values of E. For $\Lambda \neq 0$ kept constant, the 4/3 trend does not seem to be influenced by the presence of the magnetic field, below and above the limit $E_\kappa^{1/3}$.

To illustrate the importance of the anisotropy of the velocity field, mainly induced by the imposed magnetic field, we show on table 3 ratio $\widetilde{U}_s/\widetilde{U}_\phi$ as a function of Λ. The increase or decrease of the zonal wind intensity with Λ, presented in that table results from a trade-off between the decrease in $\widetilde{U}_s$ as radial motions are

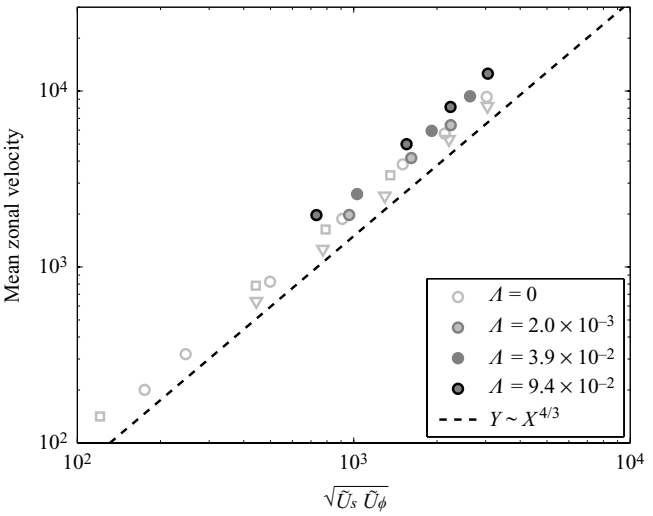

FIGURE 11. Amplitude of the mean zonal velocity $\overline{U}$ as a function of the r.m.s. velocity $(\widetilde{U}_s\widetilde{U}_\phi)^{1/2}$, obtained from numerical simulations, for $E = 1.95 \times 10^{-6}$ (circles) and various Λ. Simulations at $\Lambda = 0$ are shown for $E = 2.92 \times 10^{-6}$ (squares) and 9.74×10^{-6} (triangles). The dashed line comes from the scaling law (4.7) of Part 1.

impeded in the presence of an azimuthal magnetic field and the enhancement of the ϕ-component of the velocity. At the largest magnetic field values reached in these simulations (equivalent to $\Lambda = 0.12$), we find $\widetilde{U}_s/\widetilde{U}_\phi \simeq 0.6$, so that taking into account the anisotropy in the scaling (4.5) for $\overline{U}$ corrects by a factor of $0.6^{-2/3} \simeq 1.5$ in this specific case (i.e. a 50% correction in the zonal flow amplitude at a given $\widetilde{U}_s$). As the Elsasser number becomes closer to unity, the ratio $\widetilde{U}_s/\widetilde{U}_\phi$ decreases, so that we expect the effect of the anisotropy to become larger at larger value of Λ.

We have found numerically that the distinction between $\widetilde{U}_s$ and $\widetilde{U}_\phi$ introduced in (4.5) explains most of the variations in the zonal wind amplitude observed as we increase the magnetic field intensity. We then conclude that the general picture for the generation of zonal wind from nonlinear inertial processes, first presented in Part 1 for convection, remains valid for magnetoconvection once we take into account the anisotropy introduced in the velocity field by the imposed magnetic field.

5. Discussion

We have explored thermal convection in a rapidly rotating sphere ($E \sim 10^{-6}$) filled with liquid gallium ($P = 0.025$) permeated by a z-invariant toroidal magnetic field, with an experiment backed by a mixed quasi-geostrophic flow/three-dimensional magnetic induction numerical simulation. We have shown in Part 1 that for $P \ll 1$, differential rotation – mainly a single retrograde jet – makes up most of the kinetic energy in our experiment, even for $R \leqslant 6R_c$. This has enabled us to derive a relation between the amplitude of the r.m.s. radial and mean zonal motions, in the framework of the β-plane turbulence. According to this approach, the typical lateral extent of the jet should increase with the convective forcing (reverse cascade).

Adding a magnetic field and increasing its intensity, we note a decrease of the convective and zonal motions. In the experimental range of parameters, the effect is explained by taking into account the impact of the toroidal magnetic field on

the critical parameters only. The increase of R_c with Λ in the weak-field case, estimated from our calculations, explains the diminution of the r.m.s. velocity. From our numerical study of the onset (and in qualitative agreement with the asymptotics, see Soward 1979) a growth of the vortices in the azimuthal direction is expected. The anisotropy of the flow, as a result of the magnetic field geometry, is still predominant in the nonlinear regime, and requires one to distinguish the radial length scale – or Rhines scale – ℓ_β from the azimuthal length scales ℓ_ϕ. As a consequence the scaling law $\overline{U} \sim \widetilde{U}_s{}^{4/3}$, proposed for the non-magnetic convection in Part 1, is modified to $\overline{U} \sim (\widetilde{U}_s \widetilde{U}_\phi)^{2/3} \sim \widetilde{U}_s{}^{4/3} (\ell_\phi/\ell_\beta)^{2/3}$. However, the β-plane turbulence can also induce anisotropy, with cells elongated in the ϕ-direction (see for instance the Jovian vortices). Thus the modification we have introduced in the present paper, because of the imposed magnetic field geometry, could be of interest even in the non-magnetic case for strongly turbulent flows. Note also that in presence of an imposed poloidal magnetic field, both radial and zonal length scales might be affected, which makes the competition between the different processes more complex.

We have experimentally documented the nonlinear magnetoconvection in the weak-field case only. Studying the transition to magnetic modes would require an intensity of the imposed magnetic field, keeping constant the rotation rate, three times larger than what we have been able to achieve. Future magnetoconvection experiments should include a magnetic field that is strong enough to be destabilizing. The rotation rate should also be such that the wavenumber at the onset is large enough, so that an inverse cascade can be documented for supercritical convection. We note that, unfortunately, fluid metals that are good electrical conductors (sodium) are also good thermal conductors. With these liquids, we could reach larger values of the Elsasser number but the thermal Ekman number E_κ would be increased also.

The investigation of zonal flows in β-plane magnetoconvection is one step towards the study of zonal flows in self-excited fluid dynamos. Most numerical dynamos using no-slip boundary conditions present relatively weak zonal flows, which are governed by thermal wind (e.g. Aubert 2005). This is in favour of α^2 dynamos (Christensen & Aubert 2006), as opposed to $\alpha\omega$ dynamos where the zonal shear plays an important role. But one should keep in mind that numerical dynamos suffer from far too large Ekman numbers and magnetic Prandtl numbers. As a consequence they do not offer much space for several length scales to appear, thus inhibiting the complex role played by inertia (see for instance Fearn & Rahman 2004), and also precluding mechanisms such as the reverse cascade. The range of dynamics they can cover is thus limited, and they do not apply to the secular variations of the Earth's magnetic field at time scales from 10 to 1000 years.

The study of these short time-scales requires a better understanding of mechanisms such as the torsional oscillations (Dumberry & Bloxham 2003). The nonlinear dynamics in relation to the magnetic field can be inferred from both the $(\boldsymbol{u}\cdot\nabla)\boldsymbol{u}$ and the $\boldsymbol{j}\times\boldsymbol{B}$ terms, in the presence of the dominant Coriolis force. Hide (1966) derived long ago a quasi-geostrophic model of the core dynamics in the presence of a magnetic field. There is still much work to be done to understand what would replace, in the magnetic case, phenomena like the reverse cascade and its associated length scale.

We thank Philippe Cardin and Jean-Paul Masson who contributed to the transformation of the experimental set-up from a convection to a magnetoconvection configuration. NG is grateful to *École Doctorale "Terre, Univers et Environnement"* and Université Joseph Fourier (Grenoble) for the award of a studentship. This work was

supported by the program Expérimentation of CNRS/INSU. The computations were performed on the *Service Commun de Calcul Intensif de l'Observatoire de Grenoble*.

REFERENCES

Aubert, J. 2005 Steady zonal flows in spherical shell fluid dynamos. *J. Fluid Mech.* **542**, 53–67.

Aubert, J., Brito, D., Nataf, H.-C., Cardin, P. & Masson, J. 2001 A systematic experimental study of rapidly rotating spherical convection in water and liquid gallium. *Phys. Earth Planet. Inter.* **128**, 51–74.

Aurnou, J. M. & Olson, P. L. 2001 Experiments on Rayleigh-Bénard convection, magneto-convection and rotating magnetoconvection in liquid gallium. *J. Fluid Mech.* **430**, 283–307.

Brito, D. 1998 Approches expérimentales et théoriques de la dynamique du noyau terrestre. PhD thesis, Université Paris VII.

Brito, D., Cardin, P., Nataf, H.-C. & Marolleau, G. 1995 Experimental study of a geostrophic vortex of gallium in a transverse magnetic field. *Phys. Earth Planet. Inter.* **91**, 77–98.

Brito, D., Cardin, P., Nataf, H.-C. & Olson, P. 1996 Experiments on Joule heating and the dissipation of energy in the Earth's core. *Geophys. J. Intl* **127**, 339–347.

Brito, D., Nataf, H.-C., Cardin, P., Aubert, J. & Masson, J. 2001 Ultrasonic Doppler velocimetry in liquid gallium. *Exps. Fluids* **31**, 653–663.

Busse, F. 1970 Thermal instabilities in rapidly rotating systems. *J. Fluid Mech.* **44**, 441–460.

Busse, F. H. & Finocchi, F. 1993 The onset of thermal convection in a rotating cylindrical annulus in the presence of a magnetic field. *Phys. Earth Planet. Inter.* **80**, 13–23.

Cardin, P. & Olson, P. 1995 The influence of a toroidal magnetic field on thermal convection in the core. *Earth Planet. Sci. Lett.* **132**, 167–181.

Chandrasekar, S. 1954 The instability of a layer of fluid heated bellow and subject to the simultaneous action of a magnetic field and rotation. *Proc. R. Soc. Lond.* A **225**, 173–184.

Christensen, U. R. & Aubert, J. 2006 Scaling properties of convection-driven dynamos in rotating spherical shells and application to planetary magnetic fields. *Geophys. J. Intl* **166**, 97–114.

Dumberry, M. & Bloxham, J. 2003 Torque balance, Taylor's constraint and torsional oscillations in a numerical model of the geodynamo. *Phys. Earth Planet. Int.* **140**, 29–51.

Fearn, D. R. 1979*a* Thermal and magnetic instabilities in a rapidly rotating sphere. *Geophys. Astrophys. Fluid Dyn.* **14**, 103–126.

Fearn, D. R. 1979*b* Thermally driven hydromagnetic convection in a rapidly rotating sphere. *Proc. R. Soc. Lond.* A **369**, 227–242.

Fearn, D. R. & Rahman, M. M. 2004 The role of inertia in models of the geodynamo. *Geophys. J. Intl* **158**, 515–528.

Galperin, B., Nakano, H., Huang, H.-P. & Sukoriansky, S. 2004 The ubiquitous zonal jets in the atmospheres of giant planets and Earth's ocean. *Geophys. Res. Lett.* **31**, doi:10.1029/2004GL019691.

Gillet, N. 2004 Magnéto-convection dans une sphère en rotation rapide: approches experimentale et numérique de la convection dans les noyaux planetaires. PhD thesis, Université Joseph-Fourier (Grenoble I).

Gillet, N., Brito, D., Jault, D. & Nataf, H.-C. 2007 Experimental and numerical studies of convection in a rapidly rotating spherical shell. *J. Fluid Mech.* **580**, 83–121.

Gillet, N. & Jones, C. A. 2006 The quasi-geostrophic model for rapidly rotating spherical convection outside the tangent cylinder. *J. Fluid Mech.* **554**, 343–369.

Hide, R. 1966 Free hydromagnetic oscillations of the Earth's core and the theory of geomagnetic secular variations. *Phil. Trans. R. Soc. Lond.* A **259**, 615–646.

Jaletzky, M. 1999 Experimental study of rotating cylindrical annulus convection. PhD thesis, University of Bayreuth.

Jones, C. A., Mussa, A. I. & Worland, S. J. 2003 Magnetoconvection in a rapidly rotating sphere: the weak-field case. *Proc. R. Soc. Lond.* A **459**, 773–797.

Nagakawa, Y. 1957 Experiments on the instability of a plane layer of mercury heated from below and subject to the simultaneous action of a magnetic field and rotation. *Proc. R. Soc. Lond.* A **242**, 81–88.

Nagakawa, Y. 1958 Experiments on the instability of a plane layer of mercury heated from below and subject to the simultaneous action of a magnetic field and rotation. II. *Proc. R. Soc. Lond.* A **249**, 138–145.

Olson, P. & Glatzmaier, G. 1995 Magnetoconvection in a rotating spherical shell: structure of the flow in the outer core. *Phys. Earth Planet. Inter.* **92**, 109–118.

Or, A. C. & Busse, F. 1987 Convection in a rotating cylindrical annulus. Part 2. Transitions to asymmetric and vacillating flow. *J. Fluid Mech.* **174**, 313–326.

Petry, M., Busse, F. & Finocchi, F. 1997 Convection in a rotating cylindrical annulus in the presence of a magnetic field. *Eur. J. Mech.* B/*Fluids* **16(6)**, 817–833.

Read, P. L., Yamazaki, Y. H., Lewis, S. R., Williams, P. D., Miki-Yamazaki, K., Sommeria, J., Didelle, H. & Fincham, A. 2004 Jupiter's and Saturn's convectively driven banded jets in the laboratory. *Geophys. Res. Lett.* **31**, 22701

Rhines, P. B. 1975 Wave and turbulence on a beta-plane. *J. Fluid Mech.* **122**, 417–443.

Roberts, P. H. 1968 On the thermal instability of a self-graviting fluid sphere containing heat sources. *Phil. Trans. R. Soc. Lond.* A **263**, 93–117.

Schnaubelt, M. & Busse, F. H. 1992 Convection in a rotating cylindrical annulus. Part 3. Vacillating and spatially modulated flows. *J. Fluid Mech.* **245**, 155–173.

Secco, R. A. & Schloessin, H. H. 1989 The electrical resistivity of solid and liquid Fe at pressures up to 7 GPa. *J. Geophy. Res.* **94**, 5887–5894.

Shew, W. & Lathrop, D. P. 2005 Liquid sodium model of geophysical core convection. *Phys. Earth Planet. Inter.* **153**, 136–149.

Soward, A. 1979 Convection driven dynamos. *Phys. Earth Planet. Inter.* **20**, 134–151.

Wijs, G. D., Kresse, G., Vocadlo, L., Dobson, D., Alfè, D., Gillan, M. J. & Price, G. D. 1998 The viscosity of liquid iron at the physical conditions of the earth's core. *Nature* **392**, 805–807.

Zhang, K. 1999 Nonlinear magnetohydrodynamic convective flows in the Earth's fluid core. *Phys. Earth Planet. Inter.* **111**, 93–105.

Zhang, K., Weels, M. & Roberts, P. 2004 Effect of electrically conducting walls on rotating magnetoconvection. *Phys. Fluids* **16**, 2023–2032.